


## Revealing the stress signature and ion origin of metal plating in rechargeable batteries

Amit Chanda<sup>a</sup>, Abdulrahman Alfadhli<sup>a</sup>, Vijay A. Sethuraman<sup>b,c</sup>, Daniel P. Abraham<sup>d</sup>, Siva P.V. Nadimpalli<sup>a,\*</sup> 

<sup>a</sup> Department of Mechanical Engineering, Michigan State University, 428 S. Shaw Lane, East Lansing, MI 48824, USA

<sup>b</sup> Department of Chemical Engineering, University of South Carolina, Columbia, SC 29208, USA

<sup>c</sup> Faraday Laboratory LLC, Columbia, SC 29201, USA

<sup>d</sup> Chemical Sciences and Engineering Division, Argonne National Laboratory, Lemont, IL 60439, USA

### ARTICLE INFO

#### Keywords:

Metal plating

Stress measurement to detect plating

Na- and Li-ion batteries

Sources of ions at plating onset

### ABSTRACT

Metal plating remains a critical challenge in rechargeable batteries, directly impacting cell lifetime and safety. Understanding the underlying mechanism of plating and its early detection is essential for the safe operation of batteries. In this work, real-time stress evolution was monitored during electrochemical cycling in a range of working electrodes differing in material (graphite, hard carbon, and Ge), geometry (composite vs. solid binderless thin film), chemistry (Li-ion and Na-ion), and electrochemical reaction mechanism (intercalation and alloying). Three half-cell systems, Na–hard carbon (Na–HC), Li–graphite (Li–Gr), and Na–germanium (Na–Ge), were studied using the substrate-curvature method to quantify in-situ stress evolution during plating. In all systems, a distinct stress reversal coincided with the onset of plating, representing a universal mechanical signature of the process. The stress response revealed that (i) a two-stage plating mechanism exists and (ii) ions from both the electrolyte and host matrix contribute to initial metal deposition, a phenomenon not captured by existing models. This coupling between stress and electrochemical response provides a powerful diagnostic tool for detecting plating onset and offers new mechanistic insight into ion transport during metal deposition. These findings establish a framework for developing more accurate models of plating and improving the reliability and safety of rechargeable batteries.

### 1. Introduction

Rechargeable (secondary) batteries have become indispensable components of the modern energy infrastructure due to their high energy density, long cycle life and scalability across applications ranging from consumer electronics to electric vehicles and electricity grid storage. Continued progress in these technologies is driven by the demand for faster charging, improved safety and longer lifetimes. Among these, the ability to fast charge is particularly critical for electric vehicle applications [1,2]. However, fast charging imposes steep electrochemical and gradients within electrodes, which can drive the undesired plating of metallic species on the anode surface. Even trace amounts of plated metal can degrade cell performance through loss of active material inventory and solid electrolyte interphase (SEI) formation. The metallic deposits can become mossy or dendritic, blocking ion transport and potentially bridging the electrodes, leading to short circuits and thermal

runaway [3–5]. Understanding and detecting plating is therefore essential for designing safe, fast-charging batteries.

The fundamental mechanism of metal plating has been widely examined, especially in Li- and Na- ion systems [6–8]. In a conventional half-cell configuration, solvated cations migrate towards the working electrode, desolvate, and enter the active particles via intercalation or alloying. Under certain conditions, such as low temperature, fast charging, or overcharging [9], the cell potential can drop below 0 V versus the metal reference and the reduction of cations to their metallic state becomes thermodynamically favorable: the newly formed metal then deposits on the electrode surface rather than intercalate into (or react with) the host structure.

A broad range of diagnostic techniques has been employed to detect and characterize plating. Electrochemical measurements, such as voltage-time profiles, differential capacity analysis and impedance spectroscopy can reveal characteristic nucleation peaks or voltage

\* Corresponding author.

E-mail address: [sivan@msu.edu](mailto:sivan@msu.edu) (S.P.V. Nadimpalli).

<https://doi.org/10.1016/j.ensm.2026.104921>

Received 15 November 2025; Received in revised form 11 January 2026; Accepted 22 January 2026

Available online 24 January 2026

2405-8297/© 2026 Elsevier B.V. All rights are reserved, including those for text and data mining, AI training, and similar technologies.

plateaus associated with metal deposition [8,10,11]. Optical and video microscopy have directly visualized Li and Na plating morphologies in half-cells [6,8,12], while operando dilatometry [13,14], acoustic ultrasound [15] and impedance spectroscopy [16] based methods have been used to probe associated mechanical and interfacial changes. Operando nuclear magnetic resonance (NMR) spectroscopy provides additional insights by differentiating between metallic and ionic species and by identifying the onset of plating [7]. Despite these advances, most existing approaches primarily detect the presence or morphology of the plated metal but do not elucidate the ionic source of the deposited species. It remains unclear whether the plated metal originates exclusively from the electrolyte or whether ions may also be extracted from the active material. Furthermore, the electrochemical measurement techniques are often constrained by rate dependence and the need for near-equilibrium conditions [13], while NMR provides limited information on ion origin and transfer [7]. Consequently, the mechanistic question of coupling between the ion source and ion transport during plating remains unresolved.

The substrate-curvature method offers a complementary approach to address this challenge. This technique is widely used to measure in-situ stress evolution during electrochemical cycling [17–20] and provides unique insights into ion storage mechanisms, phase transformations and mechanical properties of electrode materials. Stress-based measurements have been successfully applied to both thin-film [18,21–23] and composite [24,25] electrodes undergoing intercalation or alloying reactions. However, the stress response associated with metal plating has not been systematically investigated. Because plating involves not only electrochemical reduction but also volumetric and interfacial changes at the electrode surface, its onset and progression are expected to produce distinct stress signatures. These signatures could serve as a sensitive probe for identifying the onset of plating and for discerning whether the ions originate from the electrolyte or from the host material.

In this work, we introduce an operando substrate-curvature based approach to study metal plating in Li- and Na- ion battery systems. Measurements were conducted on sodium-hard carbon (Na-HC), lithium-graphite (Li-Gr), and sodium-germanium (Na-Ge) cells. By simultaneously tracking electrode stress and potential during galvanostatic cycling, we identify characteristic stress signatures corresponding to the onset of plating: our approach can distinguish between contributions from electrolyte-derived ions and those extracted from the

active material. The analysis uncovers how plating-induced stresses evolve with electrode chemistry, structure and cycling conditions, thereby highlighting the coupling between electrochemical and mechanical processes during metal plating. Overall, this work establishes a new diagnostic framework for probing ion transfer and interfacial phenomena, with implications for the design of safer and faster-charging rechargeable battery systems.

## 2. Experimental methods

Fig. 1 shows the schematic of a custom-designed Teflon beaker cell equipped for *operando* substrate-curvature measurements. The three electrode configurations investigated are summarized in Table 1. Two Na-ion cells employed (i) a hard carbon (HC) composite and (ii) a Ge thin film as the working electrodes, each paired with a Na metal counter/reference electrode. The third cell used a commercial graphite (Gr) composite electrode as the working electrode and Li metal as the counter/reference electrode. These systems collectively enable comparison of plating behavior across adsorption/insertion, alloying, and intercalation reaction mechanisms.

Details of electrodes used for our experiments are shown in Table S1. Briefly, the HC composite electrode consisted of 94.8 wt % hard carbon powder, 3.2 wt % polymer binder (1.2 wt % sodium carboxymethyl cellulose and 2.0 wt % styrene-butadiene rubber), and 2.0 wt % Super P conductive additive, coated on an aluminum current collector. The Gr composite electrode comprised 93.2 wt % graphite powder, 4.3 wt % polymeric binder (1.8 wt % CMC and 2.5 wt % SBR), and 2.5 wt % Super P, coated on copper foil. Both electrodes were bonded to single-

**Table 1**  
Electrode configurations used in this study.

Cell chemistry	Working electrode	Reference electrode	Types of working electrode	Reaction mechanism
Na-ion	Hard Carbon (HC)	Na foil	Composite	Adsorption, insertion, pore-filling
Na-ion	Germanium (Ge)	Na foil	Thin film	Alloying
Li-ion	Graphite (Gr)	Li foil	Composite	Intercalation

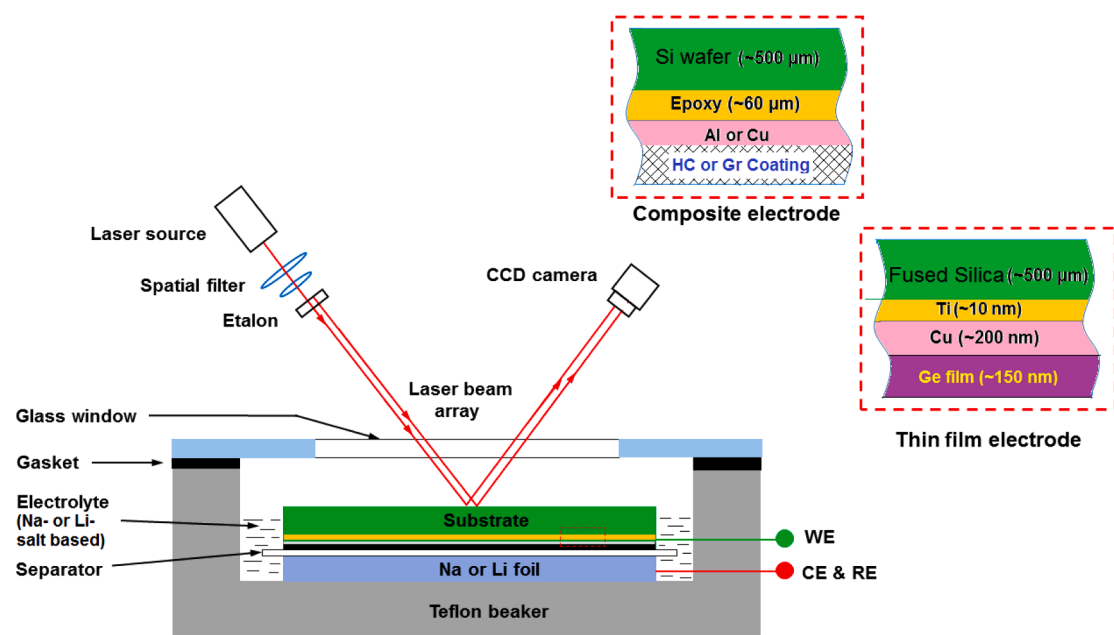


Fig. 1. Schematic of Teflon beaker cell used for operando substrate-curvature measurements. The electrode-substrate assemblies are shown in the insets (top right).

side-polished Si (111) substrates (diameter  $\approx$  50.8 mm, thickness  $\approx$  500  $\mu\text{m}$ , with thermal oxide layer) using an epoxy adhesive to enable substrate-curvature measurements. The Ge thin films (thickness  $\approx$  155 nm) were deposited on double-side-polished fused silica substrates (diameter  $\approx$  50.8 mm, thickness  $\approx$  500  $\mu\text{m}$ ) using DC magnetron sputtering at 65 W and 3 mTorr Ar pressure. Prior to Ge deposition, a 5 nm Ti adhesion layer and a 200 nm Cu current collector were sequentially deposited by e-beam evaporation. The resulting Ge electrodes were solid films without binder or conductive additives, providing a clean model system for studying plating-induced stress evolution.

The Na-ion cells used an electrolyte of 1 M sodium perchlorate ( $\text{NaClO}_4$ ) in propylene carbonate (PC) containing 5 wt % fluoroethylene carbonate (FEC) and a glass-fiber separator. The Li-ion cell employed 1 M  $\text{LiPF}_6$  in a 1:1:1 (v/v/v) mixture of ethylene carbonate (EC), diethyl carbonate (DEC), and dimethyl carbonate (DMC) with a polyethylene separator. All cells were assembled and cycled inside an argon-filled glovebox (MBraun Inc.) with  $\text{O}_2$  and  $\text{H}_2\text{O}$  levels below 1 ppm. The HC and Gr composite electrodes were soaked in the respective electrolytes for at least 12 h prior to electrochemical testing to ensure full wetting.

Electrochemical cycling was performed in the custom beaker cell. The HC composite and Ge thin-film electrodes were sodiated and desodiated galvanostatically between 2.0 and 0.0005 V vs.  $\text{Na}/\text{Na}^+$  at current densities of approximately 80  $\mu\text{A cm}^{-2}$  and 6  $\mu\text{A cm}^{-2}$ , respectively, during the first cycle. In subsequent cycles, the lower voltage cutoff was removed to enable plating once the active material was saturated and the potential dropped below 0 V vs.  $\text{Na}/\text{Na}^+$ . After a controlled plating step, the current was reversed to induce stripping of the plated Na, followed by desodiation of the host material. A similar protocol was applied to the graphite electrode in Li-ion configuration, which was cycled galvanostatically at 160  $\mu\text{A cm}^{-2}$  between 0.01 and 2 V vs.  $\text{Li}/\text{Li}^+$  for the first cycle, followed by plating, stripping, and delithiation sequences.

Real-time stress evolution patterns were monitored using multi-beam optical sensor (MOS) measurements (Fig. 1). The substrate curvature ( $\kappa$ ) was determined from the spacing change between reflected laser beams and can be expressed as,

$$\kappa = \frac{1}{A_m} \frac{d - d^0}{d^0}, \quad (1)$$

where  $A_m$  is the mirror constant (1.6 m, calibrated using a standard mirror of known curvature), and  $d^0$  and  $d$  are the initial and instantaneous beam spacings recorded by the CCD detector.

For thin-film electrodes, the electrode stress ( $\sigma$ ) is calculated using the Stoney equation:

$$\sigma = \frac{M_s t_s^2 \kappa}{6 t_f}, \quad (2)$$

where  $M_s$ ,  $t_s$ ,  $t_f$  are the bi-axial modulus, substrate thickness and electrode thickness, respectively. For composite electrodes, Eq. (2) is modified to account for multilayer structures [19] as,

$$\sigma = \frac{M_s t_s^2 \kappa}{6 t_f f(t_i, M_i)}, \quad (3)$$

where  $f(t_i, M_i)$  is a function of  $t_i$  and  $M_i$  which are the thickness and bi-axial modulus, respectively, of the  $i$ th layer of the multi-layered stack shown in Fig. 1. The parameters used for stress calculations for both the thin film and composite electrodes are summarized in Table 2.

The surface morphologies and elemental compositions of pristine, sodiated and plated HC electrodes were examined using scanning electron microscopy (SEM) coupled with energy-dispersive X-ray spectroscopy (EDX) at an acceleration voltage of 20 kV. Prior to analysis, samples were gently rinsed with DMC and dried inside the glovebox.

**Table 2**

Material parameters used for the stress calculations.

Parameter	Definition	Value	Comments
Si (111) wafer			
$E_1$	Young's Modulus	169 GPa	Ref. [19]
$\nu_1$	Poisson's ratio	0.26	Ref. [19]
$h_1$	Thickness	500 $\mu\text{m}$	Measured
Epoxy Adhesive			
$E_2$	Young's Modulus	4.3 GPa	Ref. [19]
$\nu_2$	Poisson's ratio	0.36	Ref. [19]
$h_2$	Thickness	60 $\mu\text{m}$	Measured
Aluminum collector			
$E_3$	Young's Modulus	67.3 GPa	Ref. [26]
$\nu_3$	Poisson's ratio	0.33	Ref. [26]
$h_3$	Thickness	16 $\mu\text{m}$	Measured
Copper collector			
$E_4$	Young's Modulus	117 GPa	Ref. [19]
$\nu_4$	Poisson's ratio	0.347	Ref. [19]
$h_4$	Thickness	200 nm	Measured
Hard carbon electrode			
$E_5$	Young's Modulus	9.65 GPa	Calculated, rule of mixture
$\nu_5$	Poisson's ratio	0.3	Calculated, rule of mixture
$h_5$	Thickness	90 $\mu\text{m}$	Measured
Graphite electrode			
$E_6$	Young's Modulus	6.36 GPa	Calculated, rule of mixture
$\nu_6$	Poisson's ratio	0.3	Calculated, rule of mixture
$h_6$	Thickness	41 $\mu\text{m}$	Measured

### 3. Results and discussion

#### 3.1. Stress evolution in HC during sodium plating

The real-time stress evolution during sodiation and desodiation of a HC electrode cycled between 2.0 and 0.0005 V vs.  $\text{Na}/\text{Na}^+$  is shown in Fig. S1a. Compressive stresses develops in the electrode during sodiation when Na-ions are inserted into HC particles, leading to particle expansion and inter-particle interactions. The stress reverses during desodiation and becomes tensile when Na-ions are extracted from the HC particles. These observation agree well with the recently reported stress measurements in HC electrodes during sodiation-desodiation cycling [17]. Here in Fig. 2a, we show the stress response during overcharge when Na metal is plated on the electrode. The stress is tensile ( $\sim$ 2 MPa) at the start of the experiment and becomes compressive during sodiation. This compressive stress increases nearly linearly in the sloping region of the potential profile: the stress value is -6.5 MPa at 0.1 V vs.  $\text{Na}/\text{Na}^+$ . Stress changes are relatively small during the early portion of the potential plateau (0.1–0.03 V) but then increases sharply as the potential decreases and the Na storage mechanisms change.

When the potential is driven below 0 V (Fig. 2b), a distinct voltage cusp appears at  $-0.029$  V vs  $\text{Na}/\text{Na}^+$  (at  $\sim$ 30 h), marking a Na-metal nucleation event. After this V-cusp, the potential stabilizes into a plateau, indicating steady plating. Although plating is expected at 0 V vs  $\text{Na}/\text{Na}^+$ , an overpotential of  $\sim$ 30 mV is required for the formation of metal nuclei. SEM images (Fig. 2c,d,e,f) acquired at various stages of cycling clearly indicate the differences between pristine, sodiated, plated, and stripped HC samples (see Section S2 of supplementary information for more details). The SEM micrograph of plated HC sample (acquired during the potential plateau, between  $\sim$ 35 h and  $\sim$ 55 h; points B–Y in Fig. 2b) confirms metallic Na deposition on HC particles (Fig. 2e), and EDX mapping (Fig. S2c) verifies the presence of Na-rich regions. The plated Na forms dendritic structures similar to those previously observed for Li plating on graphite [6]. While SEM confirmed the presence of plating, detailed structural characterization is required for a comprehensive understanding of the plating nucleation and growth process, which is beyond the scope of this study.

The potential response observed in Fig. 2b, specifically, the V-cusp followed by a voltage plateau, is thermodynamically consistent with the nucleation and growth of plated metal, and is also seen in Li-ion systems [6,27]. However, the stress evolution provides a unique and unexpected

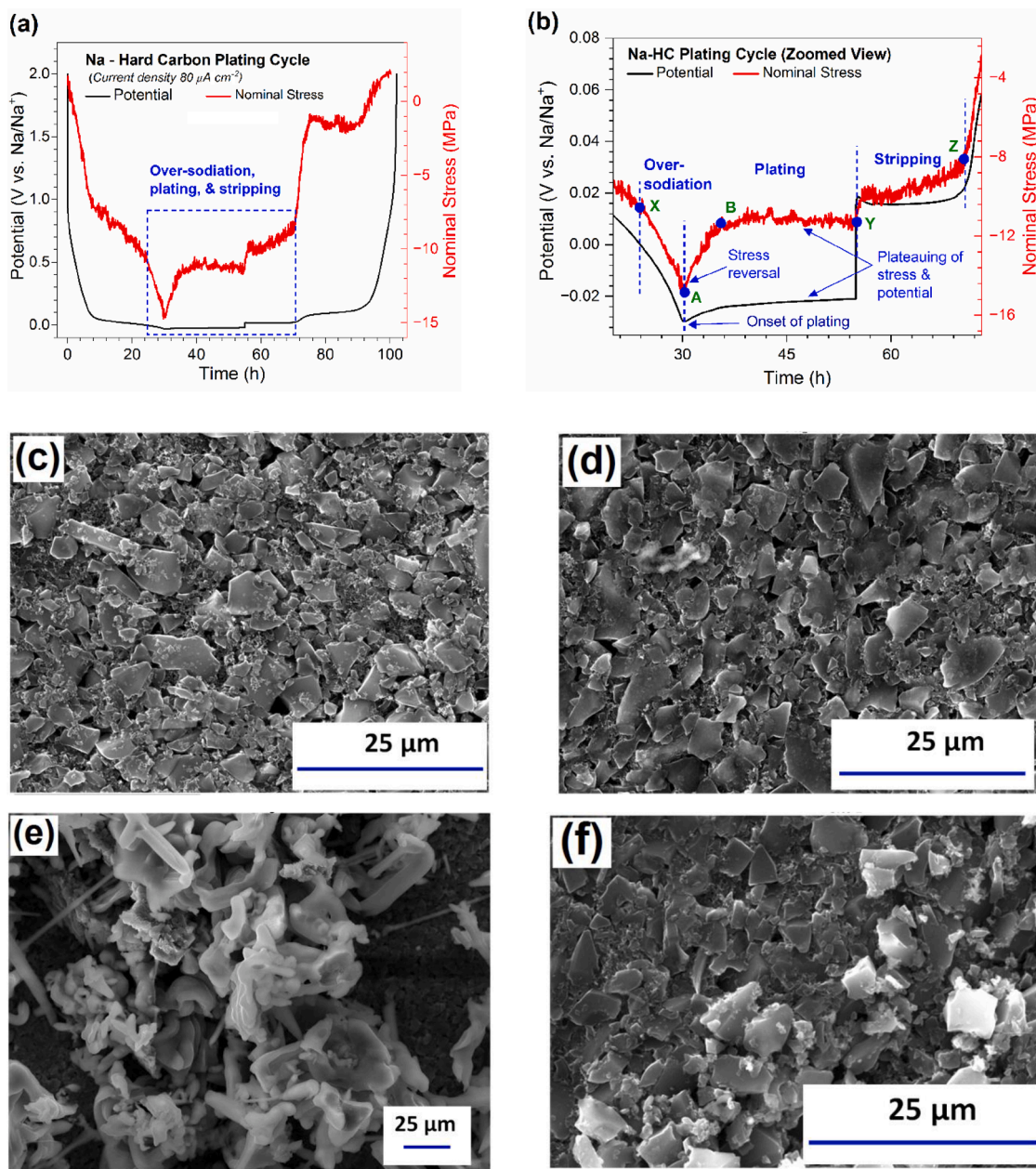


**Fig. 2.** (a) Time-dependent potential and stress profiles of the hard carbon electrode during galvanostatic cycling vs. Na, showing the onset of metal plating, stress reversal and metal stripping. (b) Expanded view of the oversodiation, plating, and stripping processes. SEM image of composite hard carbon electrodes, (c) pristine, (d) sodiated ( $>0$  V, point X in Fig. 2b), (e) after sodium plating ( $<0$  V, image was taken between point B and Y in Fig. 2b), (f) after stripping and desodiation (Fig. 2a,  $\sim 2$  V).

signature. During sodiation, the electrode stress is compressive and continues to increase with time, yet at the onset of plating ( $\sim 30$  h), it reverses direction, even though plating is still occurring. This stress reversal indicates a transient shrinkage of the active material, implying desodiation of the HC particles concurrent with the onset of plating. The stress change ( $\Delta\sigma \approx 3.29$  MPa between points A and B in Fig. 2b) corresponds to the removal of Na<sup>+</sup> ions from the HC matrix. Once plating becomes established, the stress (between B and Y) remains nearly constant, consistent with a surface process that causes negligible bulk volume changes.

These observations suggest a two-stage plating mechanism. After the onset (A–B), both electrolyte-derived Na<sup>+</sup> ions and Na<sup>+</sup> ions extracted from the HC host participate in plating, leading to transient desodiation and stress relaxation. As metallic Na deposits accumulate, they form a surface layer that blocks further ion release from the HC interior. Beyond

this threshold (B–Y), plating proceeds primarily from electrolyte-derived ions, resulting in a constant-stress plateau. This behavior is schematically illustrated in Fig. 3, which contrasts the conventional understanding—where only solvated Na<sup>+</sup> from the electrolyte contribute to plating—with the newly observed process involving ion depletion from the active material.

When the current is reversed after sufficient plating (point Y in Fig. 2b,  $\sim 55$  h), the potential immediately rises to  $+0.02$  V vs Na/Na<sup>+</sup>, halting further plating and initiating stripping. During this constant potential regime, the plated Na is progressively removed from the surface. The slight stress increase between Y and Z indicates that stripping is accompanied by partial desodiation of the underlying HC particles. After  $\sim 71$  h, once most plated Na is removed, the stress–potential behavior reverts to the pattern observed during regular desodiation. At the start of the low voltage plateau (around  $\sim 0.025$  V vs Na/Na<sup>+</sup>) the

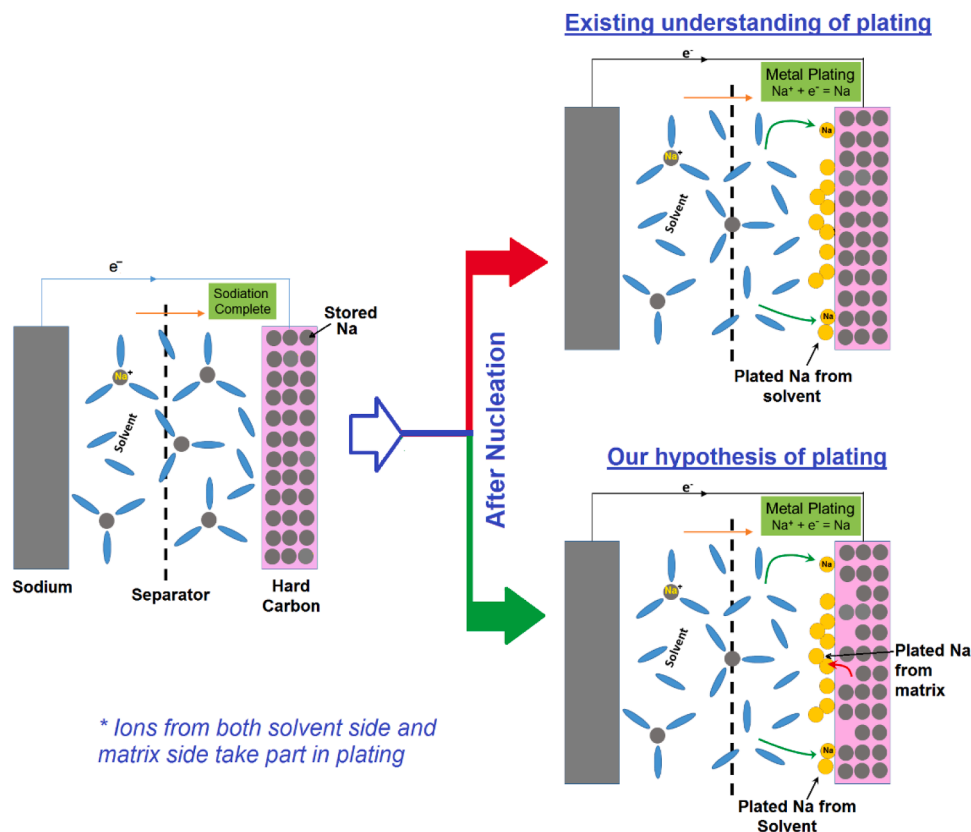


Fig. 3. Schematic representation of the proposed Na plating mechanism, illustrating ion transport and accumulation at the onset of plating. Solvated and intercalated  $\text{Na}^+$  ions are indicated in gray, and plated metallic Na is shown in yellow.

compressive stress decreases rapidly from about -7.9 MPa to -1.1 MPa, then stays roughly constant (Fig. 2a). The stress decreases further and eventually become tensile, when the potential increases from 0.1 to 2 V vs  $\text{Na}/\text{Na}^+$ , indicating a change in the desodiation mechanism.

Fig. 4a plots the potential (vs.  $\text{Na}/\text{Na}^+$ ) of the HC electrode against specific capacity, under three different rates. At slow rates ( $50$  and  $80 \mu\text{A cm}^{-2}$ ), the curves nearly overlap: the onset of plating appears at approximately between  $-0.02$  to  $-0.030$  V at  $\sim 320 \text{ mAh g}^{-1}$ . At the higher rate ( $160 \mu\text{A cm}^{-2}$ ), the electrode is strongly polarized: plating onset shifts to  $-0.045$  V and capacity is reduced to  $\sim 290 \text{ mAh g}^{-1}$ . Fig. 4b shows the corresponding nominal stress responses versus specific capacity. At the slow rates, a clear stress reversal is observed at the onset of plating (from about -15 MPa to -12 MPa). By contrast, at  $160 \mu\text{A cm}^{-2}$  the stress reversal is much smaller: instead of a distinct drop, the stress increases gradually through the plating region.

Under high current density, strong concentration gradients exist within particles and Na could accumulate near the particle surface leading to a Na-poor core and Na-rich shell. At the onset of plating under high C-rates, the ions have choice of diffusion towards the core as well as to diffuse outward to assist in plating. Besides, higher C-rates promote premature Na plating before the complete sodiation of HC particles [28]. These two aspects lead to relatively low volume change of particles under higher C-rates; hence, the absence of sharp stress reversal. At lower current densities, Na diffusion proceeds more homogeneously within HC particles; hence, at the onset of plating, relatively larger fraction of Na stored in the particle is expected to exit particles to assist in plating, leading to net volume contraction and a pronounced stress reversal. Note that the interpretation is qualitative, given the absence of independently measured parameters such as  $\text{Na}^+$  diffusivity, exchange current density ( $i_0$ ),  $\text{Na}^+$  transport and reaction kinetics.

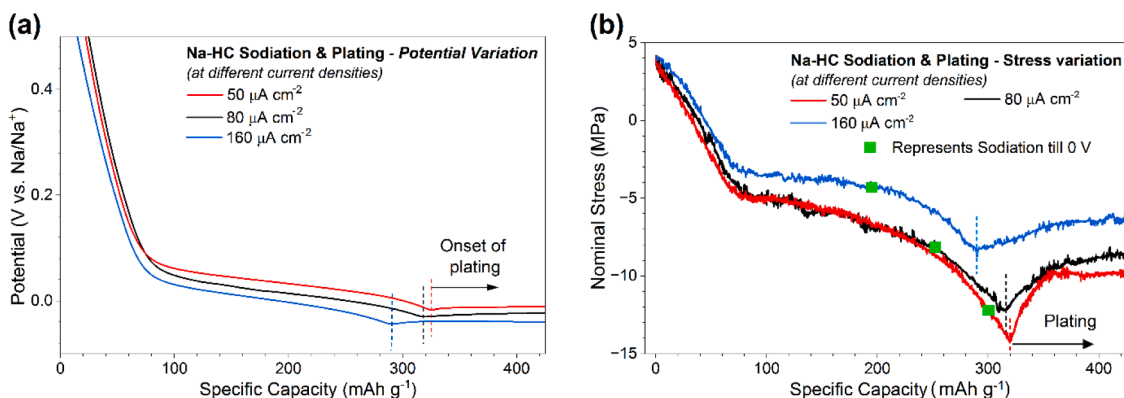


Fig. 4. (a) Potential and (b) stress evolution in the Na-HC system during galvanostatic cycling and plating at various current densities.

The stress reversal in electrodes can arise from multiple processes, including open-circuit relaxation (due to stress–potential coupling) or elastic unloading during desodiation, both of which correspond to ion extraction from the working electrode. Such behavior is evident at point Z in Fig. 2b. However, the stress reversal observed at point A in Fig. 2b occurs specifically at the onset of plating, not during OCP relaxation or desodiation. To isolate the effect of OCP relaxation, separate experiments were performed in which HC electrodes were fully sodiated and then held at open-circuit conditions prior to the onset of plating. In these tests, the magnitude of stress reversal was smaller than that observed during the actual plating process (see Fig. S3). This confirms that the stress reversal at point A cannot be attributed solely to relaxation effects. Instead, it indicates that partial desodiation occurs concurrently with the nucleation of metallic sodium, implying that both the stored  $\text{Na}^+$  ions within the HC matrix and solvated  $\text{Na}^+$  ions from the electrolyte contribute to plating during its initial stages, as illustrated schematically in Fig. 3.

In general, several processes such as side reactions (SEI), changes in interfacial adhesion, thermal expansion, and partial loss and reformation of inter-particle contacts may affect the stress evolution in battery electrodes [29,30]. However, these phenomena may not be applicable to the stress reversal observed in this study. For example, the experiments in this study were conducted under isothermal conditions, and the stress due to SEI layer was found to be negligible and leads to an increase in compressive stress, if any [18,31]. Also, since plating occurs under compressive stress [31], particles do not lose contact. To demonstrate the fact that the above-mentioned factors did not play any role in the observed stress reversal, Na plating experiment was carried out on an inert/non-reactive Al electrode along with simultaneous stress measurement under identical cycling conditions. Fig. S4 (presented in supplementary information) clearly shows that there is no stress reversal or stress change during the onset and galvanostatic plating/stripping on an inert Al electrode, strengthening the argument that the various factors mentioned above do not contribute to stress reversal and that the stress reversal observed in Figs. 2a, 4b, 5a, and 5b is due to the proposed ion depleting mechanism.

### 3.2. Plating induced ion-depletion phenomenon in other chemistries and electrodes

The hypothesis proposed above – that ions are transiently depleted from the active material to facilitate metal plating – explains both the electrochemical and mechanical signatures observed in Figs. 2a and 2b. If this phenomenon arises from fundamental processes governing metal nucleation, it should manifest regardless of battery chemistry (Li-ion, Na-ion, etc.), electrode type (composite vs. thin film), or reaction mechanism (intercalation, insertion, or alloying). To test this generality, similar cycling protocols comprising regular galvanostatic cycling followed by plating/stripping, were performed for (i) different battery

chemistries (Li and Na), (ii) different electrode materials (hard carbon, graphite, and Ge), and (iii) different electrode architectures (composite vs. binder-free thin film).

Figs. 5a and 5b show the stress response during Li plating on the graphite composite electrode and Na plating on the binder-free Ge thin film, respectively. The stress response during their regular (i.e., no plating) galvanostatic cycling, shown in Figs. S1b and S1c, agrees with previous studies [19,22]; hence, only the plating cycle is discussed here. Both systems exhibit a characteristic stress peak (point A) at the onset of plating, followed by a partial relaxation (A–B) and a subsequent stress plateau as plating progresses. This behavior is similar to that observed in the Na–HC system, suggesting that plating-induced ion depletion from the host lattice is a universal feature of metal plating processes across chemistries, electrode materials, and reaction mechanisms.

Although the qualitative trends are similar, the magnitudes of stress reversal ( $\Delta\sigma$  from A to B) differ, reflecting variations in stiffness and microstructural characteristics of electrodes. The  $\Delta\sigma$  values are  $\sim 4.5$  MPa for the Li–Gr composite,  $\sim 3.29$  MPa for the Na–HC composite, and significantly larger ( $\sim 50$  MPa) for the Na–Ge thin film. The porous composite electrodes are compliant and accommodate volumetric changes more readily for a given change in concentration (or capacity), thereby resulting in smaller stress variations. In contrast, the fully dense Ge thin film is stiffer and leads to higher change in stress reversal for a given change in concentration during elastic unloading.

An interesting distinction between the electrodes is that the Ge thin film did not produce a distinct stripping plateau during desodiation, in either the potential or stress response (Fig. 5b). The apparently different stripping behavior observed in different electrode systems can be attributed to their different ion-storage mechanisms, plating and stripping process, electrode geometry, and microstructure. For example, the metallic Li to  $\text{Li}^+$  (or Na to  $\text{Na}^+$ ) conversion during stripping happens at a well-defined potential (see Fig. 2 and 5a, revised manuscript) and shows a clear stripping plateau [32]. However, the stripping in sodiated Ge occurs under a broad range of potentials, and it occurs simultaneously with desodiation showing sloping potential (i.e., no distinct voltage plateau, Fig. 5b), with longer time indicating combined stripping and de-sodiation (e.g., de-sodiation time was 4.1 h in regular Na-Ge cycle vs. 5.1 h in plating cycle, see Fig. 5b and Fig. S1b).

### 3.3. Estimation of the number of ions depleted from active material during plating

From the above discussion, it is evident that ions exit the active particles at the onset of plating. It is instructive, however, to quantify the fraction of ions drawn from the host matrix during this process. Below we describe a general method, illustrated using data from Fig. 2b, that can be applied to any electrode system studied here.

We define the charge associated with the plating between points A and B in Fig. 6 as,

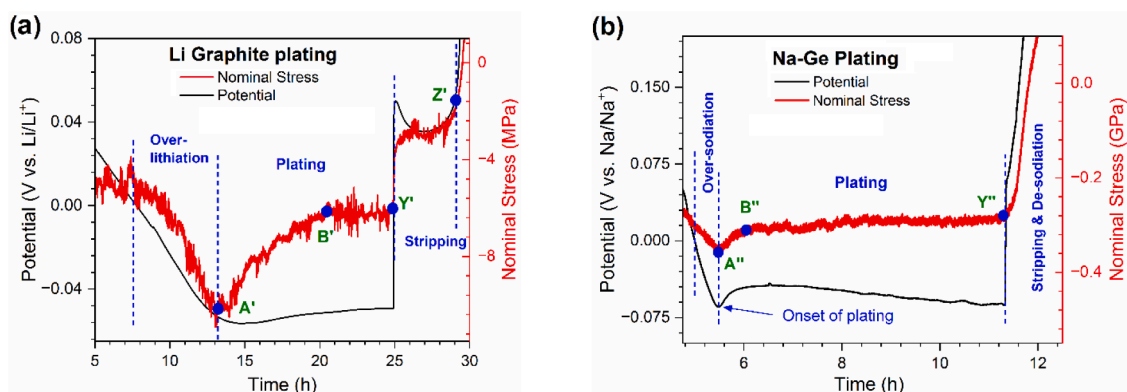
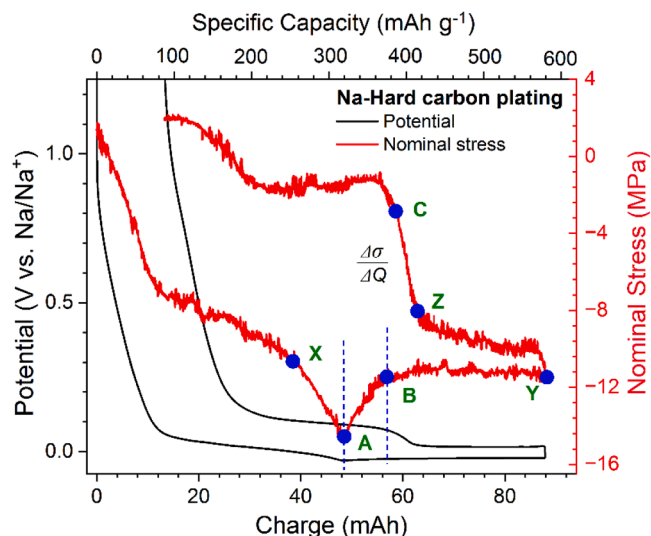


Fig. 5. Potential and stress evolution in (a) composite graphite (vs. Li) and (b) a thin film germanium electrode (vs. Na) as function of time during metal plating.



**Fig. 6.** Potential–stress response of the Na–HC electrode during the plating cycle as a function of charge, (and specific capacity) showing variations in charge and stress during plating.

$$Q_{AB}^p = Q_{AB}^a + Q_{AB}^d \quad (4)$$

where  $Q_{AB}^p$  represents the total charge delivered during the plating interval (A→B),  $Q_{AB}^a$  is the applied charge (measured directly), and  $Q_{AB}^d$  is the charge corresponding to ion depletion from the active material (i.e., ions leaving the host material to assist plating). The subscript “AB” denotes the interval from point A to point B in Fig. 6a. Although plating continues from A → Y, the stress reversal, our proxy for ion extraction from the host, occurs only during A → B.

In Eq. (4), the applied charge  $Q_{AB}^a$  is measured directly and  $Q_{AB}^d$  is obtained from the stress measurements. We assume that the stress change during desodiation of the HC electrode is mainly from elastic unloading of the active material and that the binder contributions are negligible. The stress change per unit charge,  $\Delta\sigma/\Delta Q$ , during elastic unloading can be measured from the regions between Z and C in Fig. 6 and is determined to be  $1.95 \pm 0.51 \text{ MPa mAh}^{-1}$ . We assume that this value also applies to the stress reversal (or the elastic unloading) that occurs during A → B.

Since the stress change  $\Delta\sigma$  from A→B is 3.29 MPa, we estimate:

$$Q_{AB}^d = \frac{\Delta\sigma_{AB}}{\Delta\sigma/\Delta Q} = \frac{3.29 \text{ MPa}}{1.95 \text{ MPa mAh}^{-1}} \approx 1.68 \text{ mAh}$$

With the applied charge  $Q_{AB}^a = 8.25 \text{ mAh}$ , the fraction of charge supplied from the host matrix is:

$$\frac{Q_{AB}^d}{Q_{AB}^p} \times 100\% = \frac{1.68}{1.68 + 8.25} \times 100\% \approx 16.94\%$$

Thus, in the initial phase of plating for the Na–HC system, approximately one-sixth of the Na-ions originate from the host matrix, the rest coming from the electrolyte. Note that the non-elastic factors such as binder properties and plastic deformation of active material do not affect the elastic unloading slope. This slope mainly reflects the effective elastic stiffness of the electrode and is less sensitive to binder and the extent of plastic deformation for a given electrode.

Table 3 summarizes analogous calculations for different electrode systems and current densities. Note that uniform plating on the host particles is assumed in this analysis. The data reveal that the fraction of ions depleted from the host decreases with increasing C-rate (e.g., from ~27 % at ~C/45 to ~3.6 % at ~C/7.5 for Na–HC). A plausible explanation is that at higher current densities the  $\text{Na}^+$  flux is large, causing accumulation near the particle peripheries and limiting extraction of

**Table 3**

Parameters obtained for various material systems and current densities.

Specimen	Electrode type	Current density, $\mu\text{A cm}^{-2}$ (or C-rate)	Normalized stress change ( $\Delta\sigma/\Delta Q$ , avg. value), $\text{MPa mAh}^{-1}$	Fraction of ions extracted (%)
Na – HC	Composite	50 (~C/45)	2.24	27.02
Na – HC	Composite	80 (~C/25)	1.95	16.94
Na – HC	Composite	160 (~C/7.5)	4.41	3.60
Li – Gr	Composite	160 (~C/8)	1.14	4.97
Na – Ge	Thin film	6 (~C/5)	7656	7.81

ions from the interior of the particles (as discussed in Section 3.1). As a result, ion depletion from the host is minimal at high rates. Conversely, at lower rates (C/45, C/25) more homogeneous diffusion and smaller stress gradients allow more efficient extraction of  $\text{Na}^+$  from the host prior to plating. Additionally, the thin film (Na–Ge) system shows a smaller fraction (~7.8 %) compared to composite electrodes, likely owing to its denser structure and smaller accessible surface area for host extraction.

#### 4. Conclusions

The plating phenomena in rechargeable batteries were investigated by monitoring real-time stress evolution in working electrodes during electrochemical cycling and plating. A combination of electrode architectures (composite vs. thin film), reaction mechanisms (intercalation, pore-filling, and alloying), and chemistries (Li and Na) were examined. Specifically, in-situ substrate-curvature measurements were conducted on sodium–hard carbon (Na–HC), lithium–graphite (Li–Gr), and sodium–germanium (Na–Ge) half-cells during metal plating and stripping during galvanostatic cycling. The stress responses were correlated with electrochemical potentials and post-mortem SEM/EDX observations. Complementary analysis was performed to estimate the fraction of ions depleted from the active materials during plating. The main conclusions of this work are as follows:

- A characteristic V-shaped cusp (stress reversal) was observed simultaneously in both potential and stress profiles at the onset of plating across all electrode systems, regardless of chemistry or architecture. This distinct stress signature provides a diagnostic indicator for the initiation of plating.
- The observed stress reversal arises from a volume contraction of the active material, attributed to the possible depletion of  $\text{Li}^+$  or  $\text{Na}^+$  ions from the host matrix. Both the ions extracted from the electrode and those originating from the electrolyte may participate in plating at its onset; however, plating proceeds predominantly from the electrolyte-side ions thereafter.
- The ion-depletion behavior at plating onset was consistently observed across different systems, independent of geometry (composite vs. thin film), chemistry (Li vs. Na), active material (graphite, hard carbon, Ge, etc.), or reaction mechanism (intercalation, pore-filling, alloying).
- Charge analysis indicates that only a fraction of the total ions within the electrode are depleted from the host matrix during the initial stage of plating. This depletion likely occurs in regions near the electrode surface.

Overall, these findings provide new mechanistic insights into the early stages of metal plating in rechargeable batteries. The results clarify the origin of ions involved in plating and highlight the critical coupling between electrochemical and mechanical responses. Such understanding is essential for developing accurate predictive models of plating behavior and for guiding the design of stable, high-efficiency electrodes in next-generation battery systems.

## CRedit authorship contribution statement

**Amit Chanda:** Writing – original draft, Visualization, Validation, Methodology, Investigation, Formal analysis. **Abdulrahman Alfidhli:** Investigation. **Vijay A. Sethuraman:** Supervision, Methodology. **Daniel P. Abraham:** Writing – review & editing, Visualization. **Siva P.V. Nadimpalli:** Writing – review & editing, Supervision, Resources, Project administration, Methodology, Funding acquisition, Conceptualization.

## Declaration of competing interest

The authors declare that they have no known competing financial interests or personal relationships that could have appeared to influence the work reported in this paper.

## Acknowledgements

Authors SN and AC acknowledge the funding from Michigan State University, USA through fund# GE100815. Further, SN would like to acknowledge support from G. Glenn and Marlene D. Gardner Endowed Faculty Scholar position at the Michigan State University.

## Supplementary materials

Supplementary material associated with this article can be found, in the online version, at [doi:10.1016/j.ensm.2026.104921](https://doi.org/10.1016/j.ensm.2026.104921).

## Data availability

All the data used has been presented in the manuscript

## References

- [1] USABC, APPENDIX A - USABC goals for advanced batteries, United States, Adv. Batter. Consort. LLC. (2023). <https://uscar.org/download/246/energy-storage-system-goals/12840/low-cost-fast-charge-ev-goals.pdf>.
- [2] USABC, APPENDIX B – attributes of cell technology proposed for EVs for FY 2020 commercialization cell level attributes, United States, Adv. Batter. Consort. LLC. (2016). [http://www.uscar.org/guest/article\\_view.php?articles\\_id=85](http://www.uscar.org/guest/article_view.php?articles_id=85).
- [3] Q. Yang, M. Cui, J. Hu, F. Chu, Y. Zheng, J. Liu, C. Li, Ultrathin defective C – N coating to enable nanostructured Li plating for Li metal batteries, ACS Nano 14 (2020) 1866–1878, <https://doi.org/10.1021/acsnano.9b08008>.
- [4] J. Meng, C. Li, Planting CuGa 2 seeds assisted with liquid metal for selective wrapping deposition of lithium, Energy Storage Mater. 37 (2021) 466–475, <https://doi.org/10.1016/j.ensm.2021.02.024>.
- [5] M. Huang, Z. Yao, Q. Yang, C. Li, Batteries hot paper consecutive nucleation and confinement modulation towards Li plating in seeded capsules for durable Li-metal batteries research articles, (2021). <https://doi.org/10.1002/anie.202102552>.
- [6] T. Gao, Y. Han, D. Fraggadakis, S. Das, T. Zhou, C.N. Yeh, S. Xu, W.C. Chueh, J. Li, M.Z. Bazant, Interplay of lithium intercalation and plating on a single graphite particle, Joule 5 (2021) 393–414, <https://doi.org/10.1016/j.joule.2020.12.020>.
- [7] K. Gotoh, T. Yamakami, I. Nishimura, H. Kometani, H. Ando, K. Hashi, T. Shimizu, H. Ishida, Mechanisms for overcharging of carbon electrodes in lithium-ion/sodium-ion batteries analysed by: operando solid-state NMR, J. Mater. Chem. A 8 (2020) 14472–14481, <https://doi.org/10.1039/d0ta04005c>.
- [8] C. Uhlmann, J. Illig, M. Ender, R. Schuster, E. Ivers-Tiffée, In situ detection of lithium metal plating on graphite in experimental cells, J. Power Sources 279 (2015) 428–438, <https://doi.org/10.1016/j.jpowsour.2015.01.046>.
- [9] X. Lin, K. Khosravinia, X. Hu, J. Li, W. Lu, Lithium plating mechanism, detection, and mitigation in Lithium-ion batteries, Prog. Energy Combust. Sci. 87 (2021), <https://doi.org/10.1016/j.peccs.2021.100953>.
- [10] U. Janakiraman, T.R. Garrick, M.E. Fortier, Review—lithium plating detection methods in Li-ion batteries, J. Electrochem. Soc. 167 (2020) 160552, <https://doi.org/10.1149/1945-7111/abd3b8>.
- [11] F. Sagane, K. Ikeda, K. Okita, H. Sano, H. Sakaebe, Effects of current densities on the lithium plating morphology at a lithium phosphorus oxynitride glass electrolyte /copper thin film interface, J. Power Sources 233 (2013) 34–42, <https://doi.org/10.1016/j.jpowsour.2013.01.051>.
- [12] E. Kazyak, M.J. Wang, K. Lee, S. Yadavalli, A.J. Sanchez, M.D. Thouless, J. Sakamoto, N.P. Dasgupta, Understanding the electro-chemo-mechanics of Li plating in anode-free solid-state batteries with operando 3D microscopy, Matter 5 (2022) 3912–3934, <https://doi.org/10.1016/j.matt.2022.07.020>.
- [13] M. Bauer, M. Wachtler, H. Stöwe, J.V. Persson, M.A. Danzer, Understanding the dilation and dilation relaxation behavior of graphite-based lithium-ion cells, J. Power Sources 317 (2016) 93–102, <https://doi.org/10.1016/j.jpowsour.2016.03.078>.
- [14] B. Bitzer, A. Gruhle, A new method for detecting lithium plating by measuring the cell thickness, J. Power Sources 262 (2014) 297–302, <https://doi.org/10.1016/j.jpowsour.2014.03.142>.
- [15] C. Bommier, W. Chang, Y. Lu, J. Yeung, G. Davies, R. Mohr, M. Williams, D. Steingart, In operando acoustic detection of lithium metal plating in commercial LiCoO<sub>2</sub>/graphite pouch cells, Cell Rep. Phys. Sci. 1 (2020) 100035, <https://doi.org/10.1016/j.xcrp.2020.100035>.
- [16] S. Schindler, M. Bauer, M. Petzl, M.A. Danzer, Voltage relaxation and impedance spectroscopy as in-operando methods for the detection of lithium plating on graphitic anodes in commercial lithium-ion cells, J. Power Sources 304 (2016) 170–180, <https://doi.org/10.1016/j.jpowsour.2015.11.044>.
- [17] A. Chanda, A. Pakhare, A. Alfidhli, V.A. Sethuraman, S.P.V. Nadimpalli, Real-time measurement of sodiation induced stress in hard carbon composite electrodes, J. Power Sources 609 (2024) 234678, <https://doi.org/10.1016/j.jpowsour.2024.234678>.
- [18] S.P.V. Nadimpalli, V.A. Sethuraman, G. Bucci, V. Srinivasan, A.F. Bower, P. R. Guduru, On plastic deformation and fracture in Si films during electrochemical lithiation/delithiation cycling, J. Electrochem. Soc. 160 (2013) A1885–A1893, <https://doi.org/10.1149/2.098310jes>.
- [19] V.A. Sethuraman, N. Van Winkle, D.P. Abraham, A.F. Bower, P.R. Guduru, Real-time stress measurements in lithium-ion battery negative-electrodes, J. Power Sources 206 (2012) 334–342, <https://doi.org/10.1016/j.jpowsour.2012.01.036>.
- [20] R. Tripuraneni, S. Rakshit, S.P.V. Nadimpalli, In situ measurement of the effect of stress on the chemical diffusion coefficient of Li in high-energy-density electrodes, J. Electrochem. Soc. 165 (2018) A2194–A2202, <https://doi.org/10.1149/2.0641810jes>.
- [21] A. Mukhopadhyay, A. Tokranov, K. Sena, X. Xiao, B.W. Sheldon, Thin film graphite electrodes with low stress generation during Li-intercalation, Carbon N. Y. 49 (2011) 2742–2749, <https://doi.org/10.1016/j.carbon.2011.02.067>.
- [22] S. Rakshit, A.S. Pakhare, O. Ruiz, M.R. Khoshi, E. Detsi, H. He, V.A. Sethuraman, S.P.V. Nadimpalli, Measurement of volume changes and associated stresses in Ge electrodes due to Na/Na + redox reactions, J. Electrochem. Soc. 168 (2021) 010504, <https://doi.org/10.1149/1945-7111/abd5fc>.
- [23] V.A. Sethuraman, M.J. Chon, M. Shimshak, V. Srinivasan, P.R. Guduru, In situ measurements of stress evolution in silicon thin films during electrochemical lithiation and delithiation, J. Power Sources 195 (2010) 5062–5066, <https://doi.org/10.1016/j.jpowsour.2010.02.013>.
- [24] V.A. Sethuraman, A. Nguyen, M.J. Chon, S.P.V. Nadimpalli, H. Wang, D. P. Abraham, A.F. Bower, V.B. Shenoy, P.R. Guduru, Stress evolution in composite silicon electrodes during lithiation/delithiation, J. Electrochem. Soc. 160 (2013) A739–A746, <https://doi.org/10.1149/2.021306jes>.
- [25] Y. Zhang, Y. Luo, C. Fincher, S. McProuty, G. Swenson, S. Banerjee, M. Pharr, In-situ measurements of stress evolution in composite sulfur cathodes, Energy Storage Mater. 16 (2019) 491–497, <https://doi.org/10.1016/j.ensm.2018.10.001>.
- [26] A. Chanda, S.K. Sinha, N.V. Datla, Fiber alignment and mode-mixity effects on fracture behavior of CNF/epoxy nanocomposite adhesive joints, Compos. Part B Eng. 247 (2022) 110341, <https://doi.org/10.1016/j.compositesb.2022.110341>.
- [27] W. Mei, Y. Zhang, Y. Li, P. Zhuo, Y. Chu, Y. Chen, L. Jiang, H. Zhou, J. Sun, Q. Wang, Unveiling voltage evolution during Li plating-relaxation-Li stripping cycling of lithium-ion batteries, Energy Storage Mater. 66 (2024), <https://doi.org/10.1016/j.ensm.2024.103193>.
- [28] F. Liu, Z. Chen, Y. Li, L. Fu, Y. Sun, Sodium plating on hard carbon anodes in sodium-ion batteries: mechanisms, detection methods, and mitigation strategies, Nanoscale Horiz. (2025), <https://doi.org/10.1039/d5nh00471c>.
- [29] X. Cheng, M. Pecht, In situ stress measurement techniques on Li-ion battery electrodes : a review, Energies 10 (2017) 591, <https://doi.org/10.3390/en10050591>.
- [30] H. Wang, S.P.V. Nadimpalli, V.B. Shenoy, Inelastic shape changes of silicon particles and stress evolution at binder /particle interface in a composite electrode during lithiation / delithiation cycling, Extrem. Mech. Lett. 9 (2016) 430–438, <https://doi.org/10.1016/j.eml.2016.03.020>.
- [31] J. Hwi, X. Xiao, K. Guo, Y. Liu, H. Gao, B.W. Sheldon, Stress evolution in lithium metal electrodes, Energy Storage Mater. 24 (2020) 281–290, <https://doi.org/10.1016/j.ensm.2019.08.008>.
- [32] S. Dai, Y. Tu, L. Yan, Y. Li, M. Ma, R. Huang, Observation and suppression of metallic and metallic-like plating on hard carbon for high-performance sodium-ion batteries, Mater. Today Energy 44 (2024) 101605, <https://doi.org/10.1016/j.mtener.2024.101605>.